

REPORT DOCUMENTATION PAGE

AFRL-SR-AR-TR-05-

Public reporting burden for this collection of information is estimated to average 1 hour per response, including the time for reviewing the data needed, and completing and reviewing this collection of information. Send comments regarding this burden estimate or any reducing this burden to Washington Headquarters Services, Directorate for Information Operations and Reports, 1215 Jefferson Davis Management and Budget, Paperwork Reduction Project (0704-0188), Washington, DC 20503

0021

1. AGENCY USE ONLY (Leave blank)

2. REPORT DATE
04-01-20053. REPORT TYPE AND
Final, Jan 2002 - Dec 2004

4. TITLE AND SUBTITLE

Investigation of Microwave Attenuation in Plasma

5. FUNDING NUMBERS

F49620-02-1-0072

6. AUTHOR(S)

Joseph J.S. Shang

7. PERFORMING ORGANIZATION NAME(S) AND ADDRESS(ES)

Wright State University
3640 Colonel Glenn Hwy
Dayton, OH 45435-00018. PERFORMING ORGANIZATION
REPORT NUMBER

9. SPONSORING / MONITORING AGENCY NAME(S) AND ADDRESS(ES)

Air Force Office of Scientific Research
4015 Wilson Boulevard
Arlington, VA 22203-1954 NA10. SPONSORING / MONITORING
AGENCY REPORT NUMBER

11. SUPPLEMENTARY NOTES

20050125 140

12a. DISTRIBUTION / AVAILABILITY STATEMENT

Unclassified and unlimited distribution

12b. DISTRIBUTION CODE

UU

13. ABSTRACT (Maximum 200 Words)

The computational simulation of plasma diagnostics using microwave has been successfully accomplished by the research grant. This simulation capability is based on numerical solutions to a combination of three-dimensional Maxwell equations and the generalized Ohm's law in the time domain. The transverse electromagnetic wave of the $TE_{1,0}$ mode transmitting from an aperture antenna, propagating through plasma, and receiving by the aperture antenna is simulated by solving these governing equations. The numerical result is first validated by comparing with classic theoretical results in waveguide then systematically applies to key components of microwave attenuation measuring arrangement. In this process, the radiation pattern of microwave from a pyramidal horn antenna, the diffraction and refraction of waves at the media interface, as well as, the blackout phenomenon of microwave propagating in a weakly ionized gas are delineated. Numerical results were obtained for a range of plasma transport properties including electrical conductivity, permittivity, and plasma frequency.

The newly developed computational simulation technique has been applied to resolve the large data scattering concerns between Langmuir probes and microwave absorption measurements in the AFRL/VA Mach 5 plasma channel. It was found that the irregular and fluctuating plasma generated in the magneto-hydrodynamics hypersonic facility is the main source of the measuring discrepancy. Meanwhile the simulated results contribute to a series of successful applications of hypersonic flow control via surface plasma. This achievement is also included as a revolutionary technology program by aerospace industry.

14. SUBJECT TERMS

Plasma diagnostics, Microwave, Computing simulation

15. NUMBER OF PAGES

26

16. PRICE CODE

17. SECURITY CLASSIFICATION
OF REPORT

UU

18. SECURITY CLASSIFICATION
OF THIS PAGE

UU

19. SECURITY CLASSIFICATION
OF ABSTRACT

UU

20. LIMITATION OF ABSTRACT

UU

Final Report

Grant: F49620-02-1-0072

Investigation of Microwave Attenuation in Plasma

AFOSR Program Manager: Dr. Fariba Fahroo and Dr. John D. Schmisser

Principal Investigator: Joseph J.S. Shang

Commercial Phone: 937-775-5094 FAX: 937-775-5009

Mailing Address: Department of Mechanical and Materials Engineering

Wright State University

3640 Colonel Glenn Hwy.

Dayton, Ohio 45435-0001

E-Mail Address: joseph.shang@cs.wright.edu

Research Objectives:

- Develop fundamental knowledge and simulation procedure for microwave propagation in plasma
- Attain scientific excellence through synergism with scientific community and transfer technology among scientific disciplines for USAF need

Summary of effort:

The first-ever computational simulation of plasma diagnostics using microwave has been successfully accomplished by the research grant. This simulation capability is based on numerical solutions to a combination of three-dimensional Maxwell equations and the generalized Ohm's law in the time domain. The transverse electromagnetic wave of the $TE_{1,0}$ mode transmitting from an aperture antenna, propagating through plasma, and receiving by the aperture antenna is simulated by solving these governing equations. The numerical result is first validated by comparing with classic theoretical results in waveguide then systematically applies to key components of microwave attenuation measuring arrangement. In this process, the radiation pattern of microwave from a pyramidal horn antenna, the diffraction and refraction of waves at the media interface, as well as, the blackout phenomenon of microwave propagating in a weakly ionized gas are delineated. Numerical results were obtained for a range of plasma transport properties including electrical conductivity, permittivity, and plasma frequency.

For microwave radiating simulations, the edge diffraction at antenna aperture is captured by numerical solutions and reveals significant perturbation to the emitting microwave. The numerical solution reaffirms the observation that the physical dimensions and shape of the plasma domain is a critical parameter for diagnostics measurement. In addition, the microwave reflection at the interface of free space and weakly ionized air in most

ground-based plasma channel is found to be negligible. This finding is confirmed, in spite of known impedance mismatched at these locations.

Finally, the newly developed computational simulation technique has been applied to resolve the large data scattering concerns between Langmuir probes and microwave absorption measurements in the AFRL/VA Mach 5 plasma channel. It was found that the irregular and fluctuating plasma generated in the magneto-hydrodynamics hypersonic facility is the main source of the measuring discrepancy. Meanwhile the simulated results contribute to a series of successful applications of hypersonic flow control via surface plasma. This achievement is also included as a revolutionary technology program by aerospace industry.

Accomplishments/New Findings:

Plasma exhibits outstanding attributes at different thermodynamic states. The high-temperature plasma radiates electromagnetic waves over a broad frequency spectrum ranging from microwaves to the infrared, ultraviolet, and X-ray regions. These radiating results from the bound-bound, free-bound, free-free transitions, and in the presence of a strong magnetic field the radiation even emits from electrons spinning. Plasma diagnostics using radiation and spectral line intensity measurements have been extensively used by most traditional methods [1-3]. The comparative measurements by means of spectral line intensities have also been used to determine the electron temperature in low-temperature plasma.

An electromagnetic wave propagating in an electrically conducting medium depends strongly on its electrical conductivity and transmission frequency [4]. This salient feature of microwave attenuation in plasma has been used to measure the plasma transport property of a rocket exhaust plume and the weakly ionized gas wind tunnel. A transverse electromagnetic wave propagating in a lossy medium such as the plasma can be described as;

$$E(\mathbf{r},t) = E_0 \exp(-\alpha \mathbf{r}) \exp(i\omega t - \beta \mathbf{r}) \quad (1-1)$$

where α and β are the attenuation and phase parameter;

$$\alpha = \omega \{(\mu\epsilon/2) [(1 + (\sigma/\omega\epsilon)^2)^{1/2} - 1]\}^{1/2} \quad (1-2)$$

$$\beta = \omega \{(\mu\epsilon/2) [(1 + (\sigma/\omega\epsilon)^2)^{1/2} + 1]\}^{1/2} \quad (1-3)$$

From the wave propagation viewpoint, the characteristics of wave motion depend not only on the constitutive properties of the medium: such as the magnetic permeability μ , electrical permittivity ϵ , and electrical conductivity σ , but also the microwave frequency ω . The amplitude of the wave decays exponentially and the phase shift linearly in plasma to become the principal mechanism for determining the transport property of the plasma. However, for plasma diagnostics, added complication arises when a microwave impinges on a boundary of two media. At the interface, a part of the incident wave is reflected while another part is transmitted into the second medium. The portion of the transmitted wave is governed by the continuity of the tangential components of electric and magnetic

fields. The intrinsic impedance of the media ultimately controls the behavior of this electromagnetic field at the interface [4].

A widely used non-intrusive plasma diagnostic tool is microwave probing. In plasma diagnostics the number density of the charge particles and its collision frequency with the neutral particles are measured based on the microwave attenuation [1-3]. This unique microwave behavior in weakly ionized air is also known for the famous communication blackout phenomenon during the reentry phase either of an aerospace vehicle or an inter-planet flight. When the transmission bandwidth is greater than that of the plasma, the microwave will attenuate as it propagates through the plasma. The dissipated energy along the wave path is proportional to the electrical conductivity of the medium.

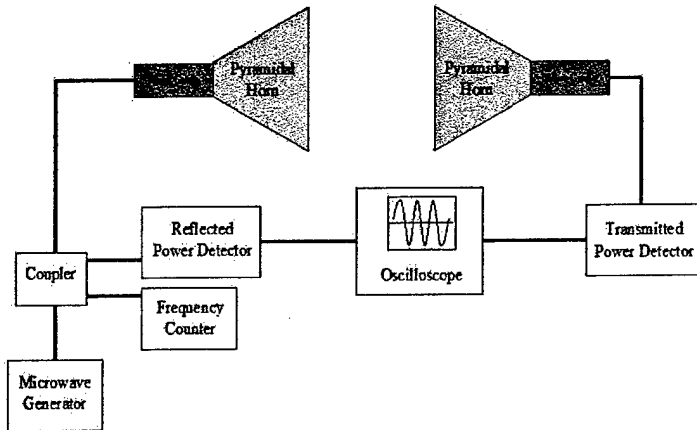


Figure 1, Experimental setup of microwave absorption measurement

In microwave probing, the wave produced by the generator is directed by a waveguide and transmitted from an antenna; the basic arrangement is depicted in Figure 1 [5,6,7]. The widely used antennae are usually a pair of pyramidal horns whose main function is to collimate the wave and reduce diffraction. The performance of these components in plasma diagnostics is also the least understood. For this reason, some fundamental and data accuracy uncertainty for plasma diagnostics remains. The evidence is clearly demonstrated by independent measurements using Langmuir probe and microwave absorption techniques [6,7]. In a hypersonic stream, the measurement discrepancy on the charged number density of a direct current glow discharge can be as high as one order of magnitude. The sources of data disparity are many; they include the explicit assumptions of the outer boundary of the plasma and negligible diffraction/refraction of the microwave. It is therefore natural to explore a numerical simulation technique to obtain a better understanding for the basic elements of microwave diagnostics.

The simulation capability for plasma microwave diagnostics is a multi-disciplinary endeavor in which the interactions between electromagnetic, fluid dynamics, and chemical kinetic properties are required. Some of the required knowledge in these disciplines is known only at the phenomenological level, the fidelity to physics is thus uncertain [8]. Nearly all low-temperature plasma generations in ground-based experimental facilities adopt the electron collision processes. The degree of ionization of the plasma is limited to 10^{-4} , which is considered to be a trace element. To alleviate these

presently irresolvable complexities, the non-equilibrium chemical kinetics is not included in the present formulation. The partial ionized gas is treated as an isotropic and homogeneous lossy medium. The validating range of the present approach will be assessed and delineated by a build-up process [9-13].

Governing Equation System

The present effort has developed a numerical simulation capability for microwave radiation from a pyramidal horn. The governing equations for the present effort are built around the solution to the three-dimensional Maxwell equations in the time domain. The closure of the partial differential equation system requires additional constitutive relationships to describe the electrical current, J , and charge density, ρ_e . The rate of change of the electrical charge density is derived from the generalized Ohm's law. The kinetic foundation of a multi-component model for the partially ionized gas is the Boltzmann equation. In a dilute gas, the collision terms in the equation are short range, so the contribution of the intermolecular collisions is practically instantaneous and localized at a point in space. However, there is no unique formulation to bridge the microscopic and the macroscopic quantity, the present analysis adopts the following approximation [9,10]:

$$\partial B / \partial t + \nabla \times E = 0 \quad (2-1)$$

$$\partial D / \partial t - \nabla \times H = -J \quad (2-2)$$

$$\nabla \cdot D = \rho_e \quad (2-3)$$

$$\nabla \cdot B = 0 \quad (2-4)$$

$$(1/\omega_{eh}) \partial J / \partial t - \sigma E + J = 0 \quad (2-5)$$

where ω_{eh} is the average collision frequency between electrons and heavy particles and σ is the electrical conductivity, $\sigma = n_e e^2 / m_e \nu$. The governing equations cast into the flux vector form in a generalized curvilinear coordinates become:

$$\partial U / \partial t + \partial F_\epsilon / \partial \epsilon + \Delta F_\eta / \partial \eta + \Delta F_\zeta / \partial \zeta = -J \quad (3-1)$$

$$F_\epsilon = F_\epsilon (\epsilon_x F_x, \epsilon_y F_y, \epsilon_z F_z) \quad (3-2)$$

$$F_\eta = F_\eta (\eta_x F_x, \eta_y F_y, \eta_z F_z) \quad (3-3)$$

$$F_\zeta = F_\zeta (\zeta_x F_x, \zeta_y F_y, \zeta_z F_z) \quad (3-4)$$

and

$$F_x = [0, -Dz/\epsilon, Dy/\epsilon, 0, Bz/\mu, -By/\mu]^T \quad (3-5)$$

$$F_y = [Dz/\epsilon, 0, -Dx/\epsilon, -Bz/\mu, 0, Bx/\mu]^T \quad (3-6)$$

$$F_z = [-Dz/\epsilon, Dx/\epsilon, 0, By/\mu, -Bx/\mu, 0]^T \quad (3-7)$$

where $\epsilon_x, \eta_y, \zeta_z$ etc are the metrics of coordinate transformation from the Cartesian (x, y, z) to a generalized curvilinear, body-oriented coordinate system (ϵ, η, ζ) .

The above differential system consists of a total of five dependent variables and two explicit constitutive relations [11,12]. For the initial/boundary value problem, the initial

value can be easily prescribed by theoretical results of the transverse electrical wave in the fundamental mode, TE_{1,0} as entrance conditions for either the waveguide or the antenna. The far-field boundary conditions are implemented through the split flux vector formulation to honor the domain of dependence [14]. In essence, at the boundaries of the computational domain, all incoming waves are suppressed using the signs of the local eigenvalue as the discriminator. On the electrically conducting surface of the waveguide and antenna, the tangential components of the electric field strength E , and the normal components of the magnetic flux density B , are continuous across the boundary. The discontinuity of the tangential components of magnetic field strength H is equal to the surface current density J_s . Finally the surface charge density ρ_s , balances the difference between normal components of the electrical displacement D , across the media interface:

$$n \times (E_1 - E_2) = 0 \quad (4-1)$$

$$n \times (H_1 - H_2) = J_s \quad (4-2)$$

$$n \cdot (B_1 - B_2) = 0 \quad (4-3)$$

$$n \cdot (D_1 - D_2) = \rho_s \quad (4-4)$$

A high-resolution, cell-centered, finite-volume, and compact-difference based high-resolution algorithms are adopted to solve the governing equations including the initial and boundary conditions. The governing equations in discrete space are [14]:

$$\Delta U / \Delta t + \Delta F_\epsilon / \Delta \epsilon + \Delta F_\eta / \Delta \eta + \Delta F_\zeta / \Delta \zeta = -J \quad (5-1)$$

For the hyperbolic partial differential equations system, the equations are easily solved by a finite-volume, splitting flux vector scheme. The split vectors on the control surface are reconstructed according to the signs of the eigenvalue to appear as:

$$F_\epsilon = F_\epsilon^+(U_L) + F_\epsilon^-(U_R) \quad (5-2)$$

$$F_\eta = F_\eta^+(U_L) + F_\eta^-(U_R) \quad (5-3)$$

$$F_\zeta = F_\zeta^+(U_L) + F_\zeta^-(U_R) \quad (5-4)$$

The challenge of an electromagnetic radiating structure simulation lies in the far-field boundary condition that is also the inherent difficulty for computational electromagnetics. The most popular approaches in the computational electromagnetics community are the absorbing boundary condition and the perfectly matched-layer scheme. The latter is actually derived from the characteristics or the domain of dependence of the hyperbolic partial differential equations system [14]. In the present split flux vector formulation, this far-field boundary condition is implemented by setting the incoming flux vector component to a null value, Equation (5).

$$F_\zeta^- = \{B_x, B_y, B_z, D_x, D_y, D_z\}^T = 0 \quad (5-5)$$

$$F_\zeta^- = \begin{vmatrix} -(\zeta_y^2 + \zeta_z^2)/2\gamma\sqrt{\epsilon\mu} & \zeta_x\zeta_y/2\gamma\sqrt{\epsilon\mu} & \zeta_x\zeta_z/2\gamma\sqrt{\epsilon\mu} & 0 & -\zeta_z/2\epsilon & \zeta_y/2\epsilon \\ \zeta_x\zeta_y/2\gamma\sqrt{\epsilon\mu} & -(\zeta_x^2 + \zeta_z^2)/2\gamma\sqrt{\epsilon\mu} & \zeta_y\zeta_z/2\gamma\sqrt{\epsilon\mu} & \zeta_z/2\epsilon & 0 & -\zeta_x/2\epsilon \end{vmatrix}$$

$$\begin{vmatrix}
\zeta_x \zeta_z / 2\gamma \sqrt{\epsilon \mu} & \zeta_y \zeta_z / 2\gamma \sqrt{\epsilon \mu} & -(\zeta_x^2 + \zeta_y^2) / 2\gamma \sqrt{\epsilon \mu} & -\zeta_y / 2\epsilon & \zeta_x / 2\epsilon & 0 \\
0 & \zeta_z / 2\mu & -\zeta_y / 2\mu & -(\zeta_y^2 + \zeta_z^2) / 2\gamma \sqrt{\epsilon \mu} & \zeta_x \zeta_y / 2\gamma \sqrt{\epsilon \mu} & \zeta_x \zeta_z / 2\gamma \sqrt{\epsilon \mu} \\
-\zeta_z / 2\mu & 0 & \zeta_x / 2\mu & \zeta_x \zeta_y / 2\gamma \sqrt{\epsilon \mu} & -(\zeta_x^2 + \zeta_z^2) / 2\gamma \sqrt{\epsilon \mu} & \zeta_y \zeta_z / 2\gamma \sqrt{\epsilon \mu} \\
\zeta_y / 2\mu & -\zeta_x / 2\mu & 0 & \zeta_x \zeta_z / 2\gamma \sqrt{\epsilon \mu} & \zeta_y \zeta_z / 2\gamma \sqrt{\epsilon \mu} & -(\zeta_x^2 + \zeta_y^2) / 2\gamma \sqrt{\epsilon \mu}
\end{vmatrix}$$

Two distinct numerical procedures were developed in the present research program. For preliminary formulation to model previously unknown and uncertain physics, the reliable temporally fourth-order and spatially third-order accurate MUSCL scheme is used [9,10]. After a complete validation process, the system of governing equations is solved by the spectral-like, high-resolution scheme with high-order, low-pass filter to suppress the parasitic spurious Fourier components contained in the numerical solution [15-17].

Numerical Procedure Validations

The attenuation parameter, α , phase shift constant, β , cutoff frequency, speed of wave propagation, and the wavelength in a waveguide are identical among the TM and TE waves. However, only the lowest order TE_{m,n} wave, TE_{1,0} has the lowest cut-off frequency and is commonly referred to as the dominant wave [4]. The subscript (m,n) represents the number of half-period variations of the field along the x and y coordinates respectively. The electric and magnetic fields within a rectangular waveguide and an aperture antenna (pyramidal horn) are selected for the purpose of validation [11,12].

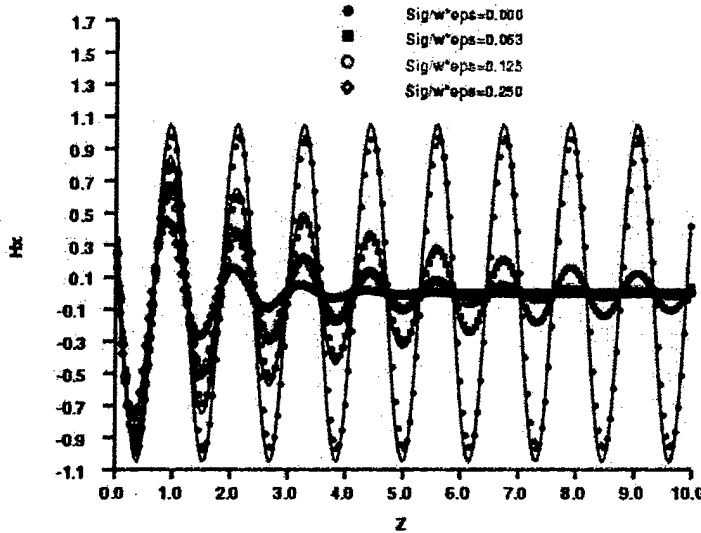


Figure 2, Validating results in waveguide, magnetic intensity H_x

The validation of the computed electrical transverse wave TE_{1,0} is accomplished by comparing with theoretical results [4,11-12]. For waveguide simulations, all numerical results were generated on a uniform mesh (25×25×197) for a square cross section

waveguide. The aspect ratio between the width and the length of the waveguide has a value of 10 and the electromagnetic wave is propagating at a frequency of 4 GHz. In Figure 2, the magnetic field components H_x of a $TE_{1,0}$ microwave wave propagating in the waveguide are compared with the theoretical results. The media within the waveguide have the normalized electrical conductivity, $\sigma/\omega\epsilon$, range from 0.0 to 0.25. The maximum discrepancy between the computed result and theory is revealed for the dielectric medium. By close examination, it was found that this deviation is easily correctable by increasing the grid-point density to a value of 22 per wavelength. The sole component of the electric field of the $TE_{1,0}$ wave D_y accompanied by the theoretic results is given in Figure 3. Similar to the previous results, the computations were performed for the media with the normalized electrical conductivity $\sigma/\omega\epsilon$ of 0.0, 0.0625, 0.125, and 0.25. Excellent agreements are reached with the theoretical results.

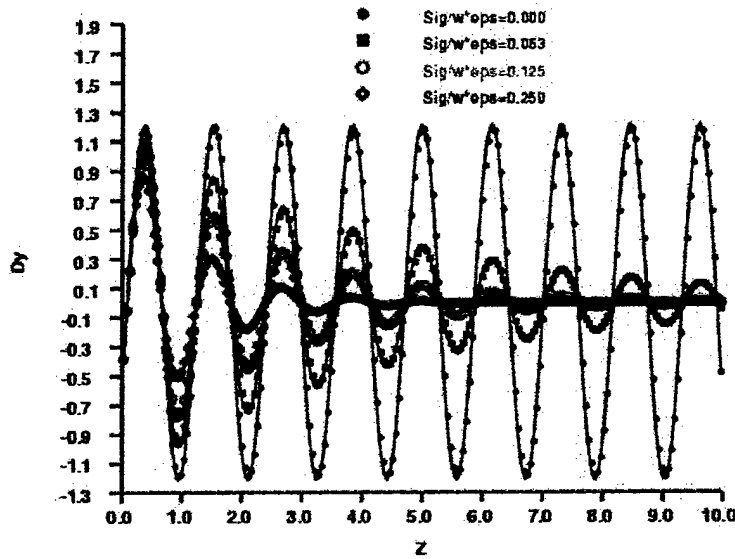


Figure 3, Validating results in waveguide, Electrical intensity D_y

All numerical simulations for the pyramidal horn are produced by the fourth-order in time and third-order in space finite-volume procedure, MUSCL. A part of this choice is made for accurately evaluating the outward normal and tangential components at the horn surface. For the present validating computations, a single mesh system of $(73 \times 25 \times 71)$ is used [11-13]. The electromagnetic field structure of the wave in the $TE_{1,0}$ mode in a pyramidal horn is given in Figure 3.

The computed electromagnetic field components and the theoretical results are compared over the entire range of the normalized electrical conductivities $0.0 < \sigma/\omega\epsilon < 0.1$. For these computations, the Neumann type of boundary condition for the normal component of magnetic intensity was imposed on the perfect electrically conducting antenna surface. This boundary condition produced a significant accuracy improvement in numerical solutions over the earlier results [9-11]. Since the present numerical simulation is a path finding effort, there is no available theoretical result for the purpose of comparison; the validation is therefore relied on the comparison with independent computations. The agreement between the numerical results by different algorithms is excellent. Figure 3

depicts the comparison of the computed and the theoretical result of a $TE_{1,0}$ wave propagating in a dielectric medium. For the essentially two-dimensional wave motion, the electrical and magnetic field variables are given in the same figure. The computed result in essence duplicates the analytic solution [18]. The maximum discrepancy measured by the L2 norm between numerical solutions by different algorithms has a magnitude less than 10^{-5} .

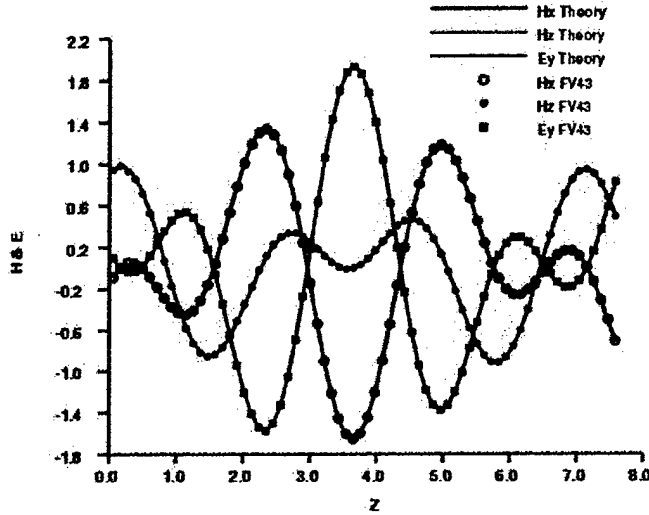


Figure 4, Validating results in pyramidal horn

According to the Poynting theorem, the numerical evaluation for the microwave attenuation is straightforward. The Poynting Vector is given as [4]:

$$\mathbf{P} = \mathbf{E} \times \mathbf{H} \quad (6-1)$$

The power flowing out of a control volume is equal to the time rate of decrease of the energy stored within the volume minus the conduction losses [4]. The instantaneous power transmitted by the microwave through plasma at any point along the beam path can be calculated by the surface integral [11,12] :

$$\iint (\mathbf{E} \times \mathbf{H}) \cdot d\mathbf{S} = -1/2 \partial \langle \epsilon \rangle / \partial t \iiint [\epsilon E^2 + \mu H^2] dV - \iiint \sigma E^2 dV \quad (6-2)$$

where $d\mathbf{S}$ is the surface vector of a control volume associated with an elementary volume dV . This instantaneous surface integral of the Poynting vector bounded by surfaces of the pyramidal horns and the cross-sections along the beam path will be performed to quantify the microwave attenuation when propagating through a lossy medium.

The power transmit by the $TE_{1,0}$ wave can be computed easily by the Poynting Vector formulation, Equation (6-1). For the dominant wave, the component of the Poynting vector along the waveguide, P_z , is depicted in Figure 5. Media of three different normalized electric conductivities, $\sigma/\omega\epsilon$ of 0.0, 0.0625, and 0.25 were simulated. For the dielectric medium, the power transmitted by the $TE_{1,0}$ wave is constant, as it should, over the entire length of the waveguide. However the electromagnetic energy is dissipated in

8.5 wavelengths in a medium with the relatively lower electric conductivity of 0.0625. At the highest electric conductivity condition simulated, $\sigma/\omega\epsilon = 0.25$, the electromagnetic energy flow essentially ceases after the wave has propagated a short distance of 2.5 wavelengths.

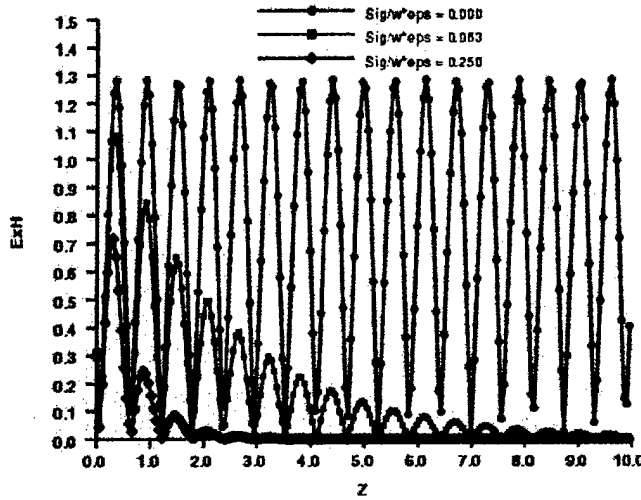


Figure 5, Poynting vector in waveguide

Radiating Field of Pyramidal Horn

The present research project also accomplished the first numerical simulation of a three-dimensional radiating structure emitting from a pyramidal horn using a generalized curvilinear coordinate transformation. A pyramidal horn generally has a rectangular cross section; at the exit plane of the horn (aperture), the height and the width of the horn are enlarged by a given ratio [12,13]. In application, only the electromagnetic wave in the $TE_{1,0}$ mode is used, because this wave has the lowest cutoff frequency of any higher order mode. The pyramidal horn is mostly utilized as a feed for reflectors and lenses, but it is also a common element of phased arrays. For this reason, the overall performance of an antenna system is often judged by its beam width and/or its directivity [18]. However, in plasma diagnostics, the total field radiated by a horn must utilize a combination of the direct field and the diffractions from the edges of its aperture. For computational microwave diagnostics, the horn edge diffraction together with the far-field boundary offers additional challenges.

In the present analysis, the microwave transmission is simulated at a frequency of 12.5 GHz (wavelength of 2.398 cm). The entrance of the pyramidal horn has the dimension in wavelengths of 0.397×0.928 , the smallest and the normalized length scale is 0.397 wavelengths (0.938cm). The horn increases its cross section linearly; its aperture has the dimensions of 3.045×3.640 wavelengths. The total length of the horn is 3.307 wavelengths. For the present investigation, two groups of computations for the microwave antenna were conducted. For each group of simulations a single mesh system was utilized.

A mesh system of $(73 \times 25 \times 71)$ is adopted for all computations within the pyramidal horn. The results from different far-field boundary conditions at the aperture of the pyramidal horn are summarized in the following. Three different boundary conditions are examined; the first calculation is based on the perfect shift condition, $U^{n+1}(i, j, k) = U^n(i, j, k-1)$. This condition is exact for a simple windward scheme when the Courant-Friederichs-Lewy (CFL) coefficient is equal to unity. The second calculation used a Neumann type of boundary condition to alleviate the reflected Fourier components at the exit boundary. A discernable improvement is indicated over that of the Dirichlet type. However, the null incoming flux condition, $F_z^-(i, j, k) = 0$, produces the best result from all of the conditions investigated [12,13].

For the complete radiating field, by taking advantage of the symmetrical property with respect to the x coordinate only the upper half space was simulation by a single mesh system of $(74 \times 5 \times 142)$. The entire three-dimensional computational domain generated by a surface-oriented coordinate transformation has the normalized physical dimensions by the minimum height of the rectangular waveguide of $(15.67 \times 6.51 \times 18.80)$. A validation of the computed electromagnetic components and the theoretical results within the pyramidal horn has been performed in an earlier effort [12]. Over the entire range of the parameter $0.0 < \sigma/\omega\xi < 0.25$, the agreement between the computational and theoretical results is reasonable while the numerical results slightly under predict the theory by 1.22 percent. The maximum discrepancy between the computed and the theoretical results is detected at the highest value of electrical conductivity. Additional grid density refinement investigation for better numerical resolution is continuing.

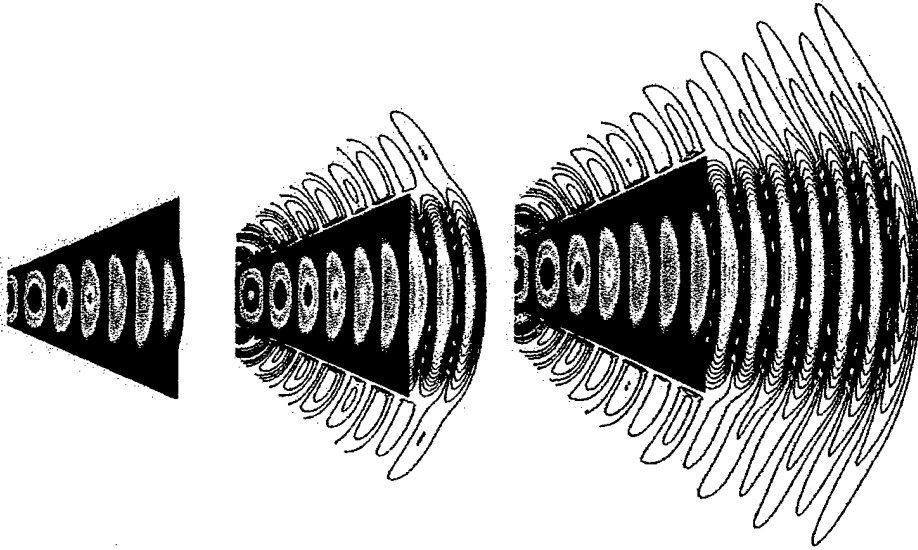


Figure 6, Radiating pattern of microwave emitted from antenna

The microwave propagation is a time-dependent phenomenon that may have a periodic asymptote. The temporal sequence of the probing microwave as it propagates from the waveguide to the far-field boundary is presented by its electrical field component, D_y . Figure 6 shows the microwave begins to emerge from the pyramidal horn into a quiescent free space. The $TE_{1,0}$ wave transmitting from the waveguide exhibits the development of

a spherical wave front within the pyramidal horn and the wavelength decreases as the wave approaches the antenna exit. As the wave completely exits into the free space, for the first time the edge diffraction at the pyramidal horn is clearly indicated. Complex wave refraction also takes place outside of the horn; the numerical result also shows that the reflected wave is not in phase with the emitting microwave within the waveguide.

The instantaneous electromagnetic field of the radiating microwave, two magnetic field components, H_x and H_z , and the sole electric field component, D_y , along the beam path are plotted together in Figure 7. All field components correctly exhibit diminishing amplitude as the radiating field expands into a greater spherical wave front. The present numerical result also shows that two key components of the Poynting vector, H_x and D_y , are completely out of phase from each other. Unfortunately, there is no known experiment available for detailed validation.

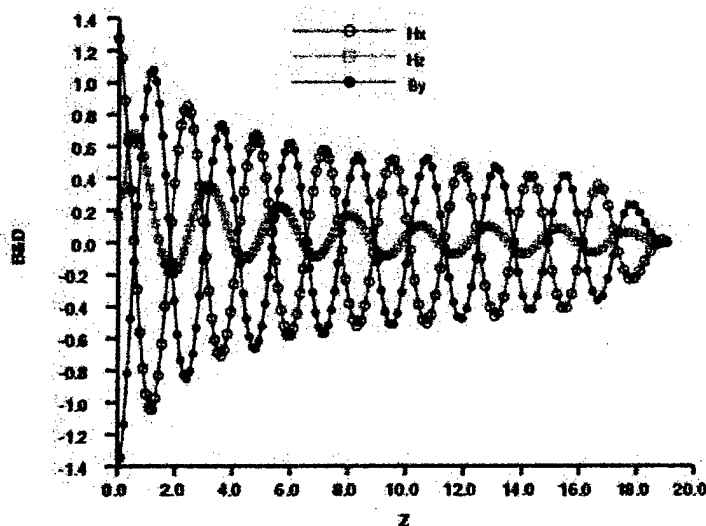


Figure 7, Instantaneous electromagnetic field of radiating microwave

The instantaneous Poynting vectors for three simulations along the beam path are depicted in Figure 8. The three computations were performed for the circumstances that the entire computational domain is either associated with free space, or microwave traverses plasma sheet of different thicknesses, $T/\lambda=0.5$ and 1.0 . The plasma sheets are characterized by a normalized electrical conductivity of $\sigma/\omega\epsilon=0.25$. In the continuously expanding structure of radiation, the Poynting vector no longer represents the dynamic range of the transmitting energy as in a constant cross section waveguide, because the energy flux density decreases with the increasing cross section of beam path. However, the different attenuations of the radiating microwaves along different beam paths are clearly demonstrated. The microwave that passes through the thicker plasma sheet incurs the greater loss of electromagnetic energy than the thinner sheet. The thickness of the plasma sheet has shown a profound effect on the microwave attenuation. A detailed comparison with the data collected from the AFRL/VA MHD channel is presently undertaken to identify the effects of microwave diffraction/refraction of the absorption technique.

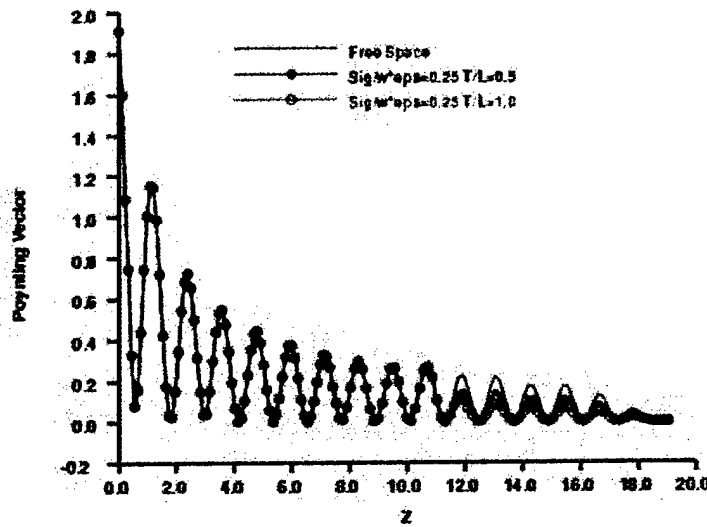


Figure 8, Poynting vector in different radiating field

Communication Blackout Phenomenon

Microwave probing is a widely used non-intrusive plasma diagnostic tool. The microwave system is adopted both for plasma diagnostics and deep-space communication. For plasma diagnostics, the number density of the charge particles and its collision frequency with the neutral particles are measured based on the microwave attenuation phenomenon [1-3]. This unique microwave behavior in weakly ionized air is also known for the famous communication blackout phenomenon during the reentry phase for either an aerospace vehicle or an inter-planet flight [12,13,19]. Communication blackout is the consequence of an incident microwave propagating at a frequency higher than the cut-off frequency, the microwave dissipating rapidly in the plasma or when the frequency matches the plasma frequency. Under the latter circumstance, the propagating wave becomes evanescent and the transmission of the electromagnetic energy ceases. When the transmission bandwidth is greater than that of the plasma, the microwave will attenuate as it propagates through the plasma. The dissipated energy along the wave path is proportional to the electrical conductivity of the medium.

An electromagnetic wave propagating in an electrically conducting medium depends strongly on its electrical conductivity and the transmission frequency. For a linear polarized plane wave traveling in a conducting medium, the current density consists of the conductive and displacement components. For an electrically neutral medium, the electric conductivity σ and the conductive current vanish, and the wave may travel without any impedance. Otherwise, the relative magnitude of σ and the product of wave frequency and electrical permittivity $\omega\xi$ will dominate the behavior of the propagating wave [4,11,12]. In the absence of an external magnetic field, the plasma can be studied as an isotropic medium. The plasma behaves as a simple quasi conductor and will support high frequency wave motion through the response of electrons.

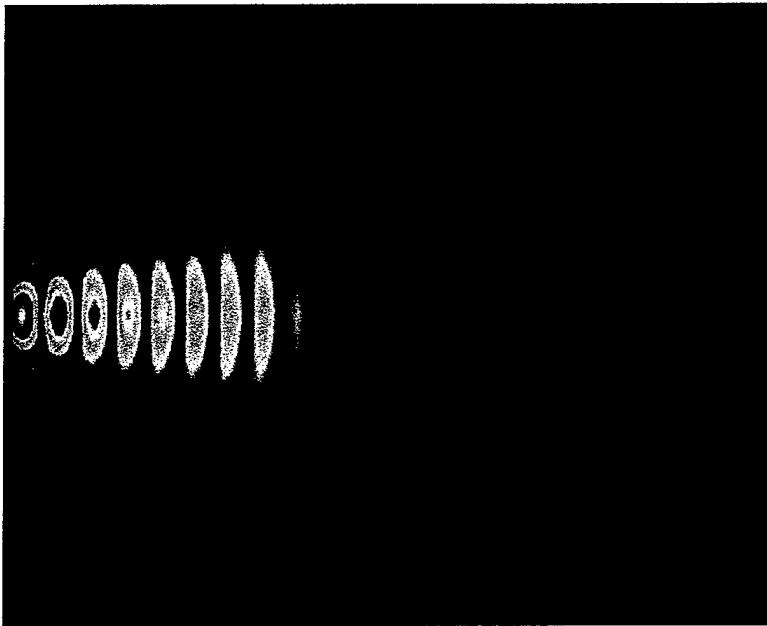


Figure 9, Microwave blackout phenomenon

The blackout phenomenon occurs for the incident microwave with a frequency of 12.5 GHz when the plasma domain is thicker than 3 wavelengths and at an electrical conductivity of 69.5 mho/m ($\sigma/\omega\epsilon=0.25$). Although all possible combinations of the plasma thickness and electrical conductivity have not been investigated at this microwave frequency, the computed contours of the electrical field intensity, E_y , clearly reveal this phenomenon in Figure 9. In fact, the microwave motion diminishes substantially in the plasma with its leading edge near the aperture of the transmitting antenna, $z/L=7.71$.

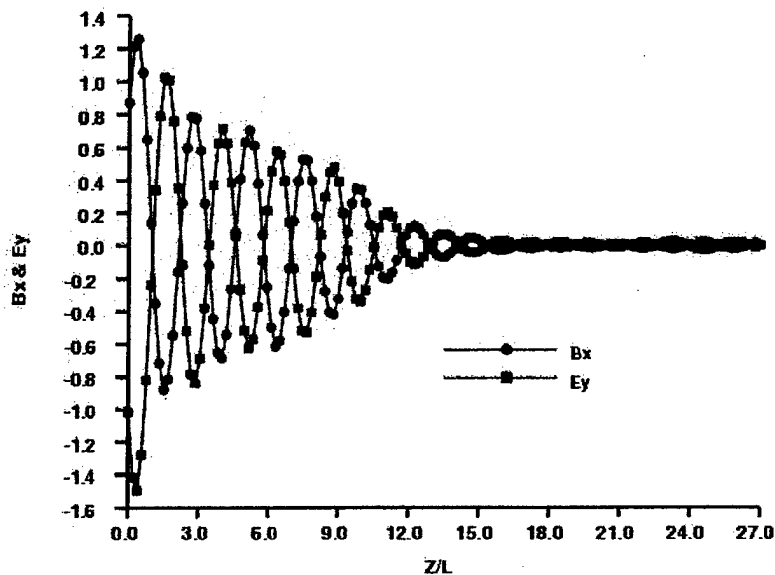


Figure 10, Electromagnetic field associated with blackout phenomenon

This observation is clearly supported by the behaviors of the instantaneous x-components of the magnetic flux density, B_x , and the y-component of the electrical intensity, E_y . The suppressed amplitudes of both the electromagnetic components of the $TE_{1,0}$ wave are clearly displayed in Figure 10. Both components essentially vanish at $z/L=14.67$ or 1.66 wavelengths from the antenna aperture. Equally important, the reflected wave at the media interface is not detected. The microwave blackout phenomenon is further substantiated by the suppressed absolute value of the Poynting vector along the beam path in Figure 11. Note that the Poynting vector essentially goes to zero at $z/L=15.00$.

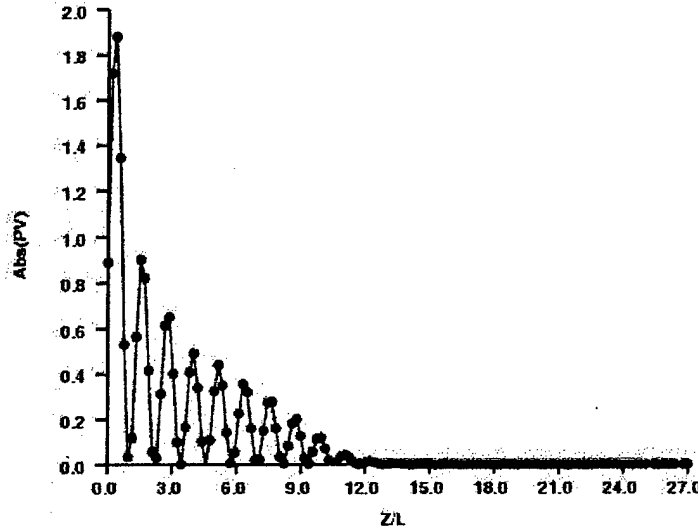


Figure 11, Poynting vector distribution along microwave path in blackout

The microwave that passes through the thicker plasma sheet suffers a greater loss of electromagnetic energy than the thinner sheet. In essence, the microwave penetration depth is proportional to the inverse square-root value of the incident wave frequency and the plasma electrical conductivity [4]. The present numerical result also demonstrated the microwave blackout phenomenon in a plasma sheet with sufficient thickness. For the investigated weakly ionized gas, the reflected wave by the unmatched impedance at the media interface is relatively unimportant [11-13].

Simulating Plasma Microwave Diagnostics

The key element of plasma diagnostics using microwave probing is a pair of pyramidal horns. Their main function is to collimate the microwave beam and to transmit and receive a microwave across a plasma medium [1-3,18]. The transport property of the weakly ionized gas is deduced from the accumulated microwave energy loss along the beam path by absorption. For accurate data reduction, the measurement may need to address the wave reflection and diffraction at multiple media interfaces [4,6]. Therefore, the numerical simulation must be built on the ability to predict the microwave dissipation and dispersion as it propagates in an electrically conducting medium. In particular, the numerical simulation also requires analyzing the electromagnetic wave propagation entering and exiting the pyramidal horns. All these capabilities have been assembled and

validated to accomplish the complete simulation of the microwave diagnostics for weakly ionized gas.

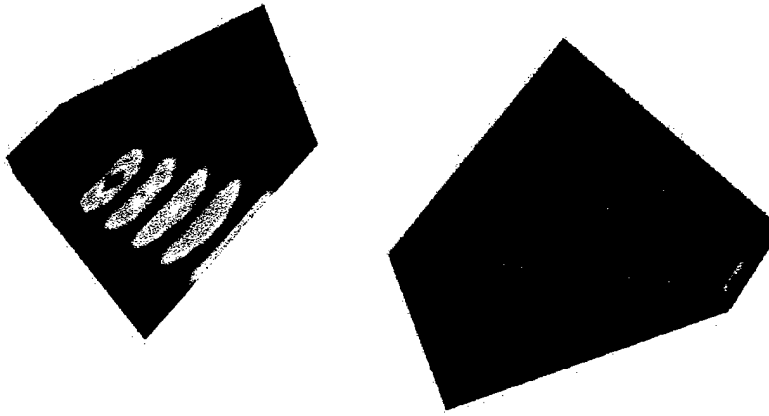


Figure 12, Simulating the experimental setup for plasma diagnostics

The basic arrangement of microwave and plasma interaction consists of a pair of antenna, usually a pyramidal horn antenna, is positioned astride the plasma domain to be measured. The microwave supplied by a signal generator is transmitted through a waveguide, then launches from the transmitting horn, and after passing through the plasma is received by another horn antenna, see Figure 12. In the present analysis, the microwave transmission is simulated at a frequency of 12.5 GHz (wavelength of 2.398 cm). The entrance of the pyramidal horn has the dimensions in wavelengths of (0.397×0.928) , the smallest and the normalized length scale is 0.397 wavelengths (0.938 cm). The horn increases its cross section linearly in both x and y directions; its aperture has the dimensions in wavelengths of (3.045×3.640) . The total length of the horn is 3.307 wavelengths. For the present investigation, three groups of computations for the microwave antenna were conducted. For each group of simulations, a single mesh system was utilized [11-13].

Taking advantage of the symmetrical property with respect to the x coordinate and the invariant property of the fundamental transverse electrical wave ($TE_{1,0}$) in the y coordinate, only the upper half space was simulated by a single mesh system of $(74 \times 5 \times 142)$ for the entire computational domain. The mesh system of the three-dimensional computational domain is generated by a surface-oriented coordinate transformation. All coordinates are normalized by the minimum height of the aperture with the dimension of $(15.74 \times 4.71 \times 26.89)$. At the simulated microwave frequency, the grid density in terms of points per wavelength is maintained at a value no less than 14. Over the entire range of the electric conductivities $0.0 < \sigma/\omega\xi < 2.0$, the agreement between results by the high-resolution and the MUSCL scheme is 1.22 percent. The maximum discrepancy between the computed results is detected at the highest value of electrical conductivity. This numerical error assessment is consistent with the previous computations for microwave propagation either in rectangular waveguides or pyramidal horns where comparisons with theoretical results are available [11,12].

The microwave propagation is a time-dependent phenomenon; in free space it is simply a harmonic motion. For the $TE_{1,0}$ wave, there are only three electromagnetic field components, the x and z components of the magnetic flux density, B_x and B_z , as well as a y-component electrical field strength, E_y . The temporal sequence of the propagating microwave as it exits from the waveguide, enters the transmitting antenna and propagates into the receiving antenna is presented by its y-component electrical field strength, E_y in Figure 13. Three features stand out; first the wave radiating from the transmitting horn is well structured and undisturbed until the wave impinges onto the exiting computational domain, and the reflected wave from the exiting boundary is insignificant. Second, the wavelength of the microwave is modified from the entrance to the aperture to reflect the wave speed differential from the waveguide to antenna exit [18]. Third, strong wave interference is easily detected in the receiving horn. The wave interaction resulting from the reflected waves from the metallic surface of the receiving antenna can also be seen. However, the edge diffractions from the antennas are not detectable from the computed results.

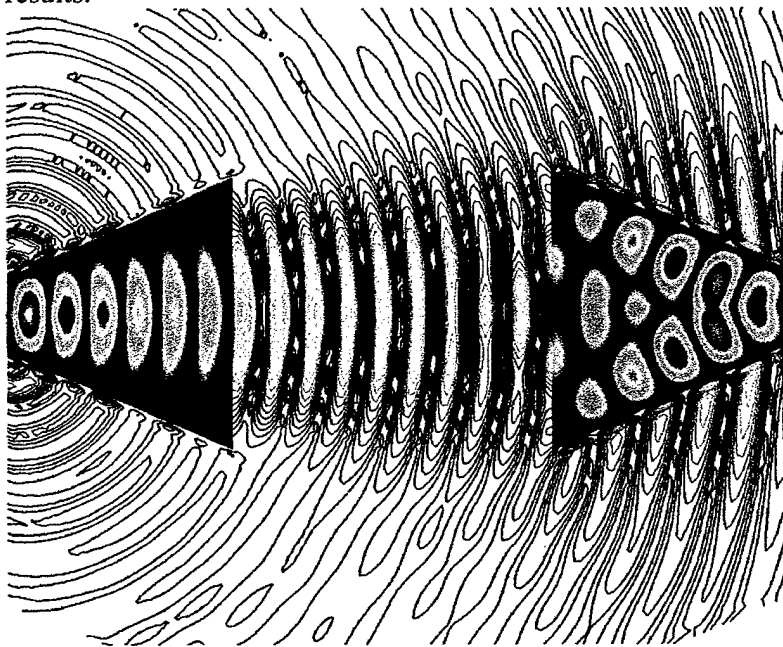


Figure 13, Electromagnetic field in plasma microwave diagnostics

In practical applications using microwaves for plasma diagnostics, the plasma is assumed to be a three-species, uniform medium, and with negligible thermal particle motion. Under this circumstance, the microwave attenuation can be studied as a function of plasma frequency, electron-neutral particle collision frequency, and transmitted frequency. It is common practice in microwave diagnostics to measure the attenuation at two or more transmitting frequencies to eliminate the error incurred in estimating the electron-neutral particle collision frequency [1-3,6].

In the data reduction process, the attenuation is evaluated by comparing the microwave power level at the receiving antenna to that in the absence of plasma. In most experiments, the microwave detector records only the voltage of the microwave [6,7].

The voltage must be converted into an average microwave power by time-integrating the converted signal after passing through a logarithmic amplifier. This data reduction process becomes a source of measurement error.

The present simulation duplicates the microwave diagnostics experimental setup in a small plasma channel operating at a Mach number of 5.15. The weakly ionized air is generated by a DC glow discharge and from a prior survey by a double Langmuir probe. The plasma stream has an electron number density and an electron temperature of $10^{12}/\text{cc}$ and 10,000 K respectively [5-7]. Microwave attenuation measurements are obtained by a previously described set of pyramidal horns across the plasma channel. The microwave transmits through quartz port windows with a thickness of 0.722 cm each, and the channel width is 2.89 cm. Therefore, the separation distance between apertures of the antenna horns is 4.33 cm. At the probing microwave frequency of 12.5 GHz, this separation distance is 1.807 wavelengths. A total of five different plasma conditions have been investigated to bracket all possible experimental conditions. Since the detailed chemical kinetics are not considered, the plasma is assigned a range of electrical conductivities from 1 to 12 mho/m to encompass the experimental conditions.

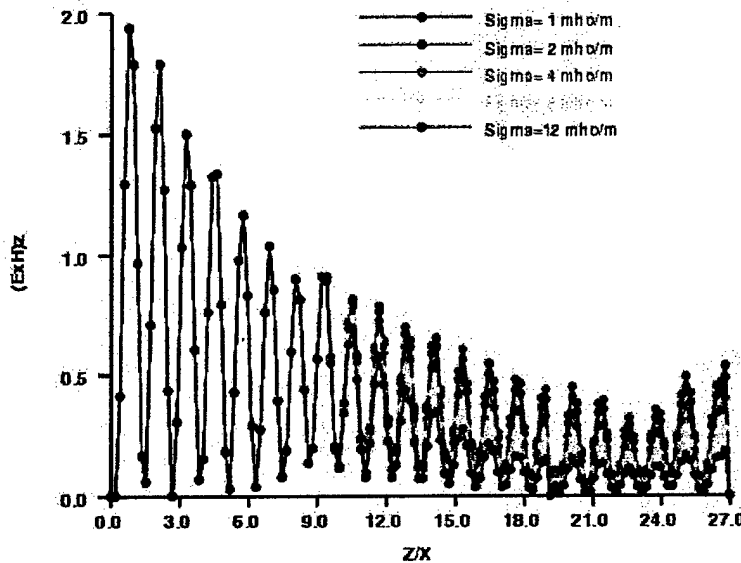


Figure 14, Poynting vector component, P_y , along the beam path

At the relatively low electrical conductivity conditions, the electromagnetic fields exhibit very little difference from the microwave propagation in free space. However, the difference in computed microwave power is clearly displayed. In Figure 14, the transmitted microwave power in free space is included as a comparing reference. It becomes evident by direct contrast to the microwave power transmission in free space that the power is continuously reflected from the radiating field and the energy is persistently dissipated in the plasma. Again, the reflected wave from the media interface is negligible, and the effects of diffraction at the apertures of antenna are accounted for but are not separable from the integrated result. Finally, the attention is focused on the

calculated microwave power within the receiving horn, in which the control volume is precisely defined.

Figure 15 depicts the microwave power distributions in the receiving horn antenna. It is easily observed in the decreasing control volume that the microwave power is significantly reduced by the reflected wave from the antenna surface. The attenuation of the microwave increases substantially with increased electrical conductivity of the plasma within the hypersonic MHD channel. The computed result of electrical conductivity of 1 mho/m agrees well with the measurements by Kurpik et al [6] and Henderson et al [7]. This agreement is unexpected, because the plasma is not uniform across the beam path. The measurement by microwave probing can yield only an averaged quantity. The computing simulation, on the other hand, assumes the medium is uniform in the MHD channel. Nevertheless, the time-averaged microwave energy of 4.2 microwatts received by the antenna is comparable to the measured data. Therefore it is reasonable to summarize that the measured data and computed result are complementary.

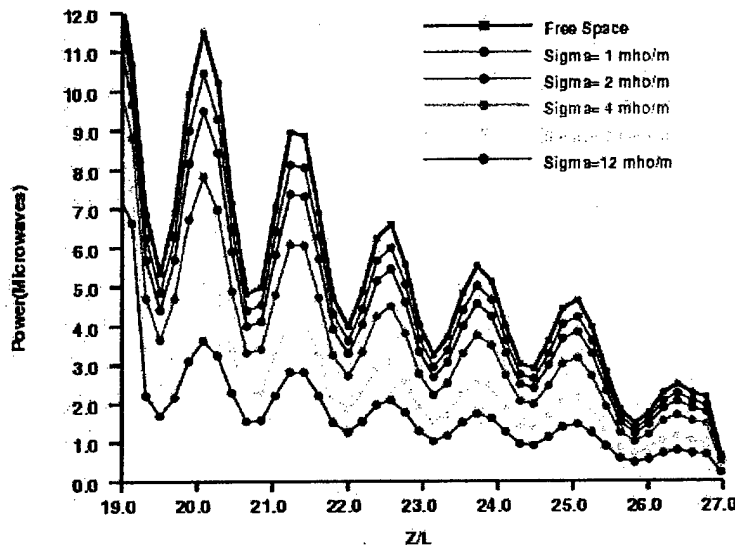


Figure 15, Microwave distributions in receiving antenna

The side-by-side presentation of the numerical result and the measurement using microwave absorption is depicted in Figure 15. The numerical result duplicates the experimental conditions of the AFRL/VA hypersonic plasma channel where the weakly ionized air is generated by a DC glow discharge across parallel plate electrodes. At the power supply for plasma generation of 1.2 kV and 250 mA, the plasma can be characterized by an electron number density up to $3 \times 10^{12}/\text{cm}^3$ and the electron temperature about 10,000 K. From the direct comparison of the computing simulation and data, the electrical conductivity weakly ionized air is determined to be in the range less than one mho/m.

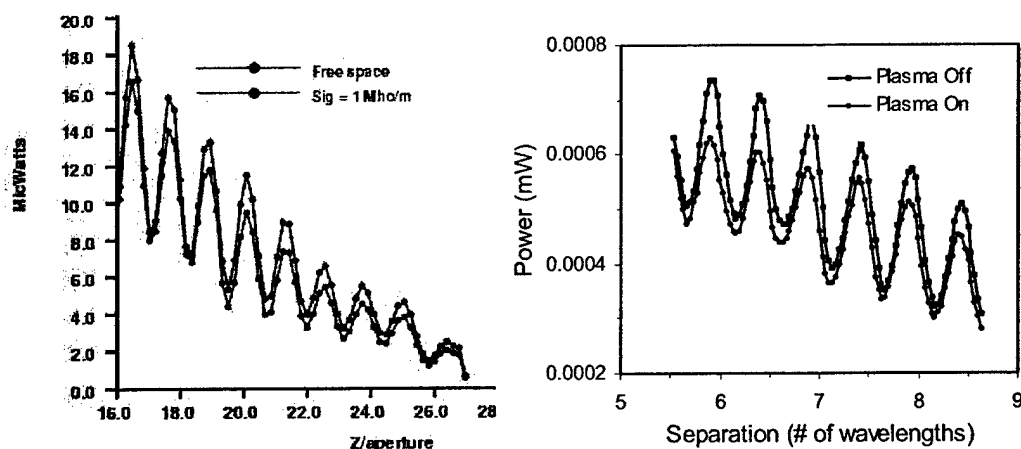


Figure 15, Side-by-side comparison for microwave power measurements

The radiating electromagnetic field for a plasma diagnostic using microwave probing has been successfully simulated by solving the time-dependent Maxwell equations and the generalized Ohm's law. The numerical simulation duplicates the aperture antenna pyramidal horns arrangement used in experiment at a transmitting frequency of 12.5 GHz. The diffractions at the apertures of the antenna and a uniform plasma column in the beam path are captured by the numerical results. For all investigated weakly ionized gases with an electrical conductivity up to 100 mho/m, the wave reflection from the interface of free space and plasma is negligible. This numerical result fully supports earlier experimental observations and reaches a reasonable affinity with experimental observations.

In Summary, the present basic research results demonstrate that a new computational simulation capability has been successfully developed and validated for plasma diagnostics. In the process of validation, the microwave communication blackout has been duplicated for the first time via a numerical simulation. Solutions of the governing equations describe in details of all diffraction and refraction phenomena in the radiating field between the transmitting and receiving aperture antennas. This newly developed technique has successfully applied to the operation and research of the AFRL/VA hypersonic plasma channel.

The research team published a total of 47 articles on plasma diagnostics and related field in plasma modeling during the reporting period. Among the public releases, eight pieces of work are archives appeared in national and international journals. Three additional efforts have also been accepted as journal articles.

References

1. Heald, M.A. and Wharton, C.B., Plasma Diagnostics with Microwaves, John Wiley and Sons, New York, 1965.
2. Golant V.E., Methods of Diagnostics Based on the Interaction of Electromagnetic Radiation with a Plasma, Basic Plasma Physics I, editors Galeev, A. and Sudan, R., North Holland Publishing Co., Amsterdam, 1983, pp. 630-680.

3. Lochte-Holtgreven, W., (edit) Plasma Diagnostics, North Holland Publishing Co., Amsterdam, 1968.
4. Krause, J.D., Electromagnetics, McGraw-Hill, 1953.
5. Shang, J.S., Kimmel, R., Hayes, J., and Tyler, C., Performance of a Low-Density Hypersonic Magneto-Aerodynamic Facility, Reno NV, 6-9 January 2003.
6. Kurpik, A., Menart, J., Shang, J., Kimmel, R., and Hayes, J., Technique for Making Microwave Absorption Measurements in a Thin Plasma Discharge, AIAA 2003-3748, Orlando, FL, 23-26 June 2003.
7. Henderson S., Menart, J., Shang J.S., Kimmel R. and Hayes J., Data Reduction Analysis for a Cylindrical, Double Langmuir Probe Operating in a High Speed Flow, AIAA 2004-0360, Reno NV, January 5-8, 2004.
8. Raizer, Yu. P., Gas Discharge Physics, Springer-Verlag, Berlin, 1991.
9. Shang, J.S., Simulating Microwave Dispersion in Weakly Ionized Air, AIAA 2003-0134, 41st Aerospace Science Meeting, Reno NV, 6-9 January 2003.
10. Shang, J.S., Computational Electromagnetics for Microwave Attenuation in Weakly Ionized Air, AIAA 2003-3621, 34th Plasmadynamics and Lasers Conference, Orlando, FL, 23-26 June 2003.
11. Shang, J.S., Simulating Microwave Diagnostics for Weakly Ionized Gas, AIAA 2004-0676, 42nd AIAA Aerospace Science Meeting, Reno NV, January 5-8, 2004.
12. Shang, J.S., Simulating Microwave Radiation for Plasma Diagnostics, AIAA 2004-2155, 35th Plasmadynamics and Lasers Conference, Portland OR, 28 June – 1 July, 2004.
13. Shang, J.S., Diffraction and Refraction in Plasma Diagnostics via Microwave Probing, AIAA 2005-0945, 43rd Aerospace Science Meeting and Exhibit, Reno NV, 10-13 January 2005.
14. Shang, J.S. and Fithen, R.M. A Comparative Study of Characteristic-Based Algorithms for the Maxwell Equations, Computational Physics, Vol. 125, 1966, pp. 378-394.
15. Lele, S.K., Compact Difference Schemes with Spectral-Like Resolution, J. Comp. Physics, Vol. 103, 1992, pp. 16-42.
16. Gaitonde, D.V. and Shang, J.S., Optimized Compact-Difference-Based Finite-Volume Schemes for Linear Wave Phenomena, J. Comp. Physics, Vol. 138, 1997, pp.617-643.
17. Shang, J.S., High-Order Compact-Difference Schemes for Time-Dependent Maxwell Equations, J. Comp. Physics, Vol. 153, 1999, pp. 312-333.
18. Maloney J., Smith, G., Thiele, E., and Gandhi, O., Modeling of Antennas, Computational Electromagnetics: The-Finite-Difference, Time-Domain Methods, Taflove, A. and Hagnes, S. (Editors), 2nd Edition, Artech House, Boston, 2002, pp. 627-701.
19. Kennet, H. and Taylor, R.A., Earth Re-entry Simulation of Planetary Entry Environment, J. Spacecraft & Rockets, Vol. 3, No. 4, 1966, pp. 504-512.

Personnel Supported:

<u>Name</u>	<u>Degree</u>	<u>Discipline</u>	<u>Involvement</u>
Shang, J.S.	PhD	Aerodynamics	75%

Hollenbaugh, Sheila	M.Sc.	Computing Science	5%
Henderson, Sean	PhD Candidate	Mechanical Engineering	25%
Stanfield, Scott	PhD Candidate	Mechanical Engineering	25%
Kurpik, Andrew	M.Sc.	Mechanical Engineering	50%
Updike, Greg	M.Sc.	Mechanical Engineering	100%
Menart, James	PhD	Mechanical Engineering	5%
Surzhikov, Sergey	PhD, D.Sc.	Computational Physics	17%
D'Ambrosio, Domenic	PhD	Aerodynamics	10%

Publications:

1. Magneto-Aerodynamic Interactions in Weakly ionized Hypersonic Flow, J.S. Shang, J.R. Hayes, J.H. Miller, and J.A. Menart, AIAA 2002-0349, January 2002.
2. Validation of Plasma Injection for Hypersonic Blunt-Body Drag Reduction, J.S. Shang, AVT Symposium on reduction of Military Vehicle Acquisition Time and Cost Through Advanced Modeling and Virtual Product Simulation, Paris France, April 22-25 2002.
3. Plasma Injection for Hypersonic Blunt-Body Drag Reduction, J.S. Shang, AIAA Journal, Vol. 36, No. 6, June 2002, pp 1178-1186.
4. Hypersonic Flow Over a Blunt Body with Plasma Injection, J.S. Shang, J. Hayes, and J. Menart, AIAA Journal of Spacecraft and Rocket, Vol. 39, No. 3, May-June 2002, pp 367-375.
5. Spike-Tipped Blunt Body in Weakly Ionized Hypersonic Stream, J.S. Shang, J. Menart, and J. Hayes, AIAA 2002-2167, 2002.
6. Spike-Tipped Blunt Body in Weakly ionized Hypersonic Stream, J.S. Shang, J.A. Menart, and J.R. Hayes, AIAA 2002-2167, 33rd Plasmadynamics and Lasers Conference, Maui HA, 20-23 May 2002.
7. Computational Electromagnetics, J.S. Shang, Sourcebook of Parallel Computing, Morgan Kaufmann Publishers, Nov. 2002, pp. 224-228.
8. A Scalable HPF Implementation of a Finite-Volume Computational Electromagnetic Application on a Cray T3E Parallel System, Y. Pan, J.S. Shang, and M. Guo, E-journal Performance Evaluation and Modelling for Computer Systems, 18, 2002, pp. 1-24.
9. Simulating Microwave Dispersion in Weakly Ionized Air, J.S. Shang, AIAA 2003-0134, 41st Aerospace Science Meeting, Reno NV, 6-9 January 2003.
10. Data Reduction Analysis for Cylindrical, Double Langmuir Probes Operating in Collisionless to Collisional, Quiescent Plasmas, J. Menart and J. Shang, AIAA 2003-0136, 41st Aerospace Science Meeting, Reno NV, 6-9 January 2003.
11. Performance of a Low-Density Hypersonic Magneto-Aerodynamic Facility, J.S. Shang, R. Kimmel, J. Hayes, and Charles Tyler, AIAA 2003-0329, 41st Aerospace Science Meeting, Reno NV, 6-9 January 2003.

12. Glow Discharge in Magnetic Field, Sergey T. Surzhikov and J.S. Shang, AIAA 2003-1054, 41st Aerospace Science Meeting, Reno NV, 6-9 January 2003.
13. Survey of Plasma Generated in a Mach 5 Wind Tunnel, J. Menart, J. S. Shang, S. Henderson, A. Kurpik, R. Kimmel, and J. Hayes, AIAA 2003-1194, 41st Aerospace Science Meeting, Reno NV, 6-9 January 2003.
14. Shared Knowledge in Computational Fluid Dynamics, Electromagnetics, and Magneto-Aerodynamics, J.S. Shang, Progress in Aerospace Sciences Vol. 38, No. 6-7, 2002, pp. 449-467.
15. Blunt Body in Hypersonic Electromagnetic Flow Field, J.S. Shang, J. Hayes, J., Menart, and J. Miller, J. of Aircraft, Vol. 40, No. 2, 2003, pp. 314-322.
16. A Scalable HPF Implementation of a Finite-Volume Computational Electromagnetics Application on a CRAY T3E Parallel System, Y. Pan, J.S. Shang, and M. Guo, Concurrency and Computation: Practice and Experience, Vol.15, No. 6, 2003, pp. 607-621.
17. Computational Electromagnetics for Microwave Attenuation in Weakly Ionized Air, J. S. Shang, AIAA 2003-3621, 34th Plasmadynamics and Lasers Conference, Orlando, FL, 23-26 June 2003.
18. Supersonic Internal Flows with Gas Discharged and External Magnetic Field, S. Surzhikov and J.S. Shang, AIAA 2003-3625, 34th Plasmadynamics and Lasers Conference, Orlando, FL, 23-26 June 2003.
19. Glow Discharge in Magnetic Field with Heating of Neutral Gas, S. Surzhikov and J.S. Shang, AIAA 2003-3654, 34th Plasmadynamics and Lasers Conference, Orlando, FL, 23-26 June 2003.
20. Technique for Making Microwave Absorption Measurements in a Thin Plasma Discharge, A. Kurpik, J. Menart, J. Shang, R. Kimmel, and J. Hayes, AIAA 2003-3748, 34th Plasmadynamics and Lasers Conference, Orlando, FL, 23-26 June 2003.
21. Numerical Simulation of Subsonic Gas Flows with Glow Discharge and Magnetic Field, S. Surzhikov and J. Shang, AIAA 2003-3759, 34th Plasmadynamics and Lasers Conference, Orlando, FL, 23-26 June 2003.
22. Measurements of a Transverse DC Discharge in a Mach 5 Flow, R. Kimmel, J. Hayes, J. Menart, J. Shang, S. Henderson, and A. Kurpik, AIAA 2003-3855, 34th Plasmadynamics and Lasers Conference, Orlando, FL, 23-26 June 2003.

23. Effects of Magnetic Fields on Plasmas Generated in a Mach 5 Wind Tunnel, J. Menart, J. Shang, R. Kimmel, and J. Hayes, AIAA 2003-4165, 34th Plasmadynamics and Lasers Conference, Orlando, FL, 23-26 June 2003.
24. A Glance Back and Outlook of Computational Fluid Dynamics, J. S. Shang, FEDSM 2003-45420, 4th ASME/JSME Joint Fluids Engineering Conference, Honolulu HA, July 2003.
25. Performance of a Low-Density Hypersonic Magneto-Aerodynamic Facility, R. Kimmel, J. Hayes, C. Tyler, and J. Shang, III Workshop of Thermochemical and Plasma Processes in Aerodynamics, St.-Petersburg, Russia, July 28-31, 2003, pp. 190-207.
26. Historical Perspective of Magneto-Fluid-Dynamics, J.S. Shang, Introduction to Magneto-Fluid-Dynamics for Aerospace Applications, Lecture Series 2004-01, von Karman Institute for Fluid Dynamics, Rhode-ST-Genese Belgium, Oct. 2003.
27. Design and Implementation of a Magnetoaerodynamic Channel, R.L. Kimmel, J. Menart, and J.S. Shang, Introduction to Magneto-Fluid-Dynamics for Aerospace Applications, Lecture Series 2004-01, von Karman Institute for Fluid Dynamics, Rhode-ST-Genese Belgium, Oct. 2003.
28. MFD Research in US Toward Aerospace Applications, J.S. Shang, Introduction to Magneto-Fluid-Dynamics for Aerospace Applications, Lecture Series 2004-01, von Karman Institute for Fluid Dynamics, Rhode-ST-Genese Belgium, Oct. 2003.
29. Physics of the Direct Current Discharge Interaction with Supersonic Gas Flow, S.T. Surzhikov, and J.S. Shang, AIAA 2004-0176, 42nd AIAA Aerospace Science Meeting, Reno NV, January 5-8, 2004.
30. Data Reduction Analysis for a Cylindrical, Double Langmuir Probe Operating in a High Speed Flow, S. Henderson, J. Menart, J.S. Shang, R. Kimmel, and J. Hayes, AIAA 2004-0360, 42nd AIAA Aerospace Science Meeting, Reno NV, January 5-8, 2004.
31. Magneto-Aerodynamic Interaction for Hypersonic Flow Control, J.S. Shang and S.T. Surzhikov, AIAA 2004-0508, 42nd AIAA Aerospace Science Meeting, Reno NV, January 5-8, 2004.
32. Effect of Surface Plasma Discharges on Boundary Layer at Mach 5, R. Kimmel, J. Hayes, J. Menart, and J.S. Shang, AIAA 2004-0509, 42nd AIAA Aerospace Science Meeting, Reno NV, January 5-8, 2004.
33. Three Decades of Accomplishments in Computational Fluid Dynamics, J.S. Shang, Progress in Aerospace Science, Vol. 40 No. 3, 2004, pp.173-197.
34. Simulating Microwave Diagnostics for Weakly Ionized Gas, J. S. Shang, AIAA 2004-0676, 42nd AIAA Aerospace Science Meeting, Reno NV, January 5-8, 2004.

35. Simulating Microwave Radiation for Plasma Diagnostics, J.S. Shang, AIAA 2004-2155, 35th Plasmadynamics and Lasers Conference, Portland OR, 28 June – 1 July, 2004.
36. Study of Surface and Volumetric Heating Effects in a Mach 5 Flow, J. Menart, S. Henderson, J. Shang, R. Kimmel, and J. Hayes, AIAA 2004-2262, 35th Plasmadynamics and Lasers Conference, Portland OR, 28 June – 1 July, 2004.
37. DC Plasma Discharge Effects on a Mach 5 Flow Between Small Plate Electrodes, J. Menart, S. Henderson, J. Shang, R. Kimmel, and J. Hayes, AIAA 2004-2262, 35th Plasmadynamics and Lasers Conference, Portland OR, 28 June – 1 July, 2004.
38. Simulating Magneto-Aerodynamic Actuator for Hypersonic Flow Control, J. Shang, D. Gaitonde, and G. Updike, AIAA 2004-2657, 35th Plasmadynamics and Lasers Conference, Portland OR, 28 June – 1 July, 2004.
39. Multi-Fluid Models of Weakly Ionized Gas Flows, S. T. Surzhikov and J. S. Shang, AIAA 2004-2659, 35th Plasmadynamics and Lasers Conference, Portland OR, 28 June – 1 July, 2004.
40. Effect of Magnetic Fields on Surface Plasma Discharges at Mach 5, R. Kimmel, J. Hayes, J. Menart, and J. Shang, 35th Plasmadynamics and Lasers Conference, Portland OR, 28 June – 1 July, 2004.
41. Drift-Diffusion Model for Magneto-Fluid-Dynamics Interaction J.S. Shang and S.T. Surzhikov, 3rd International Conference on Computational Fluid Dynamics, Toronto Canada, July 12-16 2004.
42. Hypersonic Separated Flow Control Using Magneto-Aerodynamic Interaction, G. Updike, J.S. Shang, and D. Gaitonde, AIAA 2005-0164, 43rd Aerospace Science Meeting and Exhibit, Reno NV, 10-13 January, 2005.
43. Supersonic Flow Around Wing with Localized Surface Gas Discharge, S. Surzhikov and J. Shang, AIAA 2005-0406, 43rd Aerospace Science Meeting and Exhibit, Reno NV, 10-13 January 2005.
44. Plasma Actuator for Hypersonic Flow Control, J.S. Shang, S.T. Surzhikov, R. Kimmel, D. Gaitonde, J. Menart, and J. Hayes, AIAA 2005-0562, 43rd Aerospace Science Meeting and Exhibit, Reno NV, 10-13 January, 2005.
45. Diffraction and Refraction in Plasma Diagnostics via Microwave Probing, J.S. Shang, AIAA 2005-0945, 43rd Aerospace Science Meeting and Exhibit, Reno NV, 10-13 January, 2005.

46. Application of Plasma Discharge Arrays to High-Speed Flow Control, R. Kimmel, J. Hayes, J. Menart, and J. Shang, AIAA 2005-0946, 43rd Aerospace Science Meeting and Exhibit, Reno NV, 10-13 January, 2005.

47. Total Drag and Lift Measurements in a Mach 5 Flow affected by a Plasma Discharge and a Magnetic Field, J. Menart, J. Shang, R. Kimmel, and J. Hayes, AIAA 2005-0947, 43rd Aerospace Science Meeting and Exhibit, Reno NV, 10-13 January, 2005.

Technical Transitions:

The plasma diagnostics and plasma-based hypersonic flow control techniques that developed in this effort have been incorporated by the Revolutionary Technology Programs of Skunk Works, Lockheed-Martin Corporation. Point of contact; Charles Chase, Phone: 703-324-2542.

Research results of the present effort have guided the microwave absorption measurement at the AFRL/VA Mach 5 MHD channel. Points of contact at the AFRL/VA experimental facility are Dr. Roger Kimmel AFRL/VAAA, 937-255-8295 and James Hayes AFRL/VAAC, 937-255-4246. The concept of hypersonic MHD actuator derived from the present research effort has also been shared with Dr. Roger Kimmel of AFRL/VAAA, Dr. Datta Gaitonde of AFRL/VAAC, and Dr. Terry A. Weisshaar of DARPA/DSO, 571-218-4620. The present research grant also supports the development of a subsonic MHD channel for AFRL/VA. Point of contact is Lt. Richard Derbis, AFRL/VAAA, 937-255-8674.

The developed simulation capabilities for microwave diagnostics and low-temperature modeling have been shared with the AFOSR tasks of Computational Hypersonics (2307N403 and 2307N617) and Computational Electromagnetics (2307N400). In specific, the technique of drift-diffusion theory for computing plasma transport property has been introduced to a basic research team in AFRL/VAAC. The concept of electromagnetic actuator for hypersonic flow control and its experimental set-up have also been provided to the Mach 5 low-density plasma channel in AFRL/VAAA.

The present effort maintains a very strong support for the operation of a Mach 5 low-density plasma tunnel in the Air Vehicles Directorate, Air Force Research Laboratory. The interactions with the scientific research community have also extended to reach a large sector of the aerospace community to include the Window-in-Science program of AFOSR/EOARD: Collaborating scientists of the present efforts include:

Dr. D. Gaitonde, AFRL/VA
Dr. R. Kimmel, AFRL/VA
Prof. R. MacCormack, Stanford University
Prof. D. Gottlieb, Brown University
Prof. W. Rich, Ohio State University
Prof. I. Adamovich, Ohio State University
Prof. W. Bailey, Air Force Institute of Technology
Prof. J. Menart, Wright State University
Prof. D. D'Ambrosio, Polytechnic Institute of Torino, Italy
Dr. S.P. Wilkinson, NASA LaRC

Dr. R.T. Exton, NASA LaRC
Dr. C-L. Chang, NASA LaRC
Prof. S.T. Surzhikov, Russian Academy of Science
Prof. Yu. Kolesnichenko, Russian Academy of Science

Consultative and Advisory Functions:

The principal investigator of the research grant is retained by the AFRL as an emeritus scientist to rejuvenate the aerodynamic experimental programs. He also continues his role as a member of the AIAA Plasmadynamics and Laser Technical Committee since April 1992.

NASA NIA/LaRC (National Institute of Aerospace, NASA, Langley Research Center) invited the principal investigator of the present research grant to be a visiting research scholar for their plasmadynamic R&D programs (Research Cooperative Agreement, NCC-1-02043).

New Discoveries, Inventions, or Patent Disclosures:

The plasma actuator has been successfully implemented as embedded electrodes adjacent to hypersonic leading edge configurations. The Joule heating and Lorentz force substantially modify the displacement thickness of the boundary layer with a minute amount of electric energy input (50 mA at 1.2 kV). Meanwhile the ensuing viscous-inviscid interaction in hypersonic speed significantly accentuates the induced aerodynamic force. This added physical dimension is harnessed as a flight control mechanism without any moving parts. The basic concept of the plasma actuator for flow control has been expanded to all flight regimes. The operating principle is based on the electromagnetic perturbation to flow field and subsequent amplification by inviscid-viscous interaction. This concept has received increasing support from computational simulation and experimental observations in the research community.